ACute3D: A Compact, Cost-Effective, 3-D Printed Laser Autocollimator

Qingxin Meng, Julian Stirling, William J. Wadsworth, and Richard W. Bowman

***Abstract*— The ACute3D is a compact laser autocollimator, capable of precise angle measurement in two orthogonal directions over a maximum measurement range of 7200 × 5300 arcsec. The measurement uncertainty over the middle third of its range is less than 3 arcsec. Our novel design exploits the geometric freedom of fused filament 3-D printing to realize a monolithic optomechanical assembly. The monolithic block makes the instrument compact, lightweight, stiff, and resistant to drift, as well as minimizing alignment during assembly and minimizing cost. Our openly licensed design together with our use of digital fabrication makes this autocollimator convenient to customize or integrate into larger instruments. The total bill of materials cost is around £200, making precise angle measurement available in a wide range of contexts. We demonstrate an application of the ACute3D by measuring the angular deviation of a precision linear stage, showing that our design is ready for typical laboratory use.**

***Index Terms*— 3-D printing, open source hardware, optical sensors.**

I. Introduction

AUTOCOLLIMATORS are precision instruments for optical noncontact measurement of small angles. In production environments, autocollimators are used to measure the straightness, parallelism, and squareness of machine tools and for measuring the accuracy of rotary and index tables [1]–[3]. Autocollimators can also be used in quality control to measure the flatness and parallelism of manufactured components or for the inspection of optical components, such as wedges and prisms [4]–[6]. Similarly, they are used for alignment precision scientific instrumentation and for assessing uncertainties due to Abbe error [7] or parasitic tilt [8]. They also find use in experiments, which directly measure or control angular displacement, such as torsion balances [9].

An autocollimator measures the tilt of a reflective test object by projecting a collimated beam onto the reflective surface and measuring the angle of the reflected beam. Manual autocollimators illuminate a crosshair reticle placed at the focal plane of a collimating lens, projecting the image of the crosshair to infinity. The light reflected by the target reflector is collected by the same collimating lens and imaged onto a graduated reticle [see Fig. 1(a)]. Incoming and outgoing light are separated by a beam splitter. An eyepiece is used to view the graduated reticle and the image of the first reticle. As both reticles are on the focal plane of the collimating lens, displacement between the two is only sensitive to the angle of the target reflector. By increasing the focal length of the collimating lens, the angular sensitivity of the autocollimator can be improved at the expense of measurement range. A digital autocollimator uses a similar principle, replacing the graduated reticle and eyepiece with an image sensor at the focal plane of the collimating lens [see Fig. 1(b)] [10]–[15]. Digital autocollimators have improved angular sensitivity for a given focal length as they can use digital image processing to track displacement rather than being limited by the graduations on a reticle. They can also be used to continuously monitor angle, with precision timing, over long experiments.

More recently, there has been a trend toward using a collimated laser beam as the light source [16]–[22]. In these laser autocollimators, the collimating lens is only used to focus the reflected light beam onto a photodetector. Taking advantage of the small diameter of laser beams, the size of the target reflector can be greatly reduced, providing more flexibility when integrating into experimental setups.

Although the basic structure and measurement principle have barely changed over the years, commercial autocollimators remain prohibitively expensive to even well-funded institutes. In this article, we present a highly compact, cost-effective, laser autocollimator that can be assembled and aligned in a few hours. The autocollimator uses a minimal number of easily available standard components. To mount the optical components stably and reproducibly, we have taken advantage of the geometric freedom of 3-D printers to create structures that are not possible with traditional machining. Mountings for components and baffled walls (to catch stray light) are all integrated into a single monolithic component. The monolithic construction and compact size (88 mm × 149 mm × 48 mm) compensate for the lack of rigidity of the plastic, creating a highly mechanically stable instrument. A slip-plate for camera alignment, as well as the covers and the beam dump, is printed separately.

The autocollimator was developed as open source hardware and software, with the aim to make precise angle measurement accessible to laboratories on a modest budget. The design is freely shared online in the form of parametric CAD files, meaning our autocollimator can be produced by anyone with a 3-D printer.

The 3-D printers have become a standard piece of hardware in laboratories across the globe due to the open source RepRap project [23]. The ability to quickly produce physical

Manuscript received February 7, 2022; revised April 5, 2022; accepted April 19, 2022. Date of publication May 13, 2022; date of current version May 24, 2022. This work was supported in part by the Engineering and Physical Sciences Research Council (EPSRC) under Grant EP/R013969/1, in part by the Royal Society under Grant URF\R1\180153 and Grant RGF\EA\181034, in part by the University of Bath, and in part by the Global Challenges Research Fund. The Associate Editor coordinating the review process was Dr. Rosenda Valdés Arencibia. *(Corresponding author: Qingxin Meng.)*

The authors are with the Department of Physics, University of Bath, Claverton Down, Bath BA2 7AY, U.K. (e-mail: qm237@bath.ac.uk; js3214@bath.ac.uk; pyswjw@bath.ac.uk; rwb34@bath.ac.uk).

Digital Object Identifier 10.1109/TIM.2022.3174267

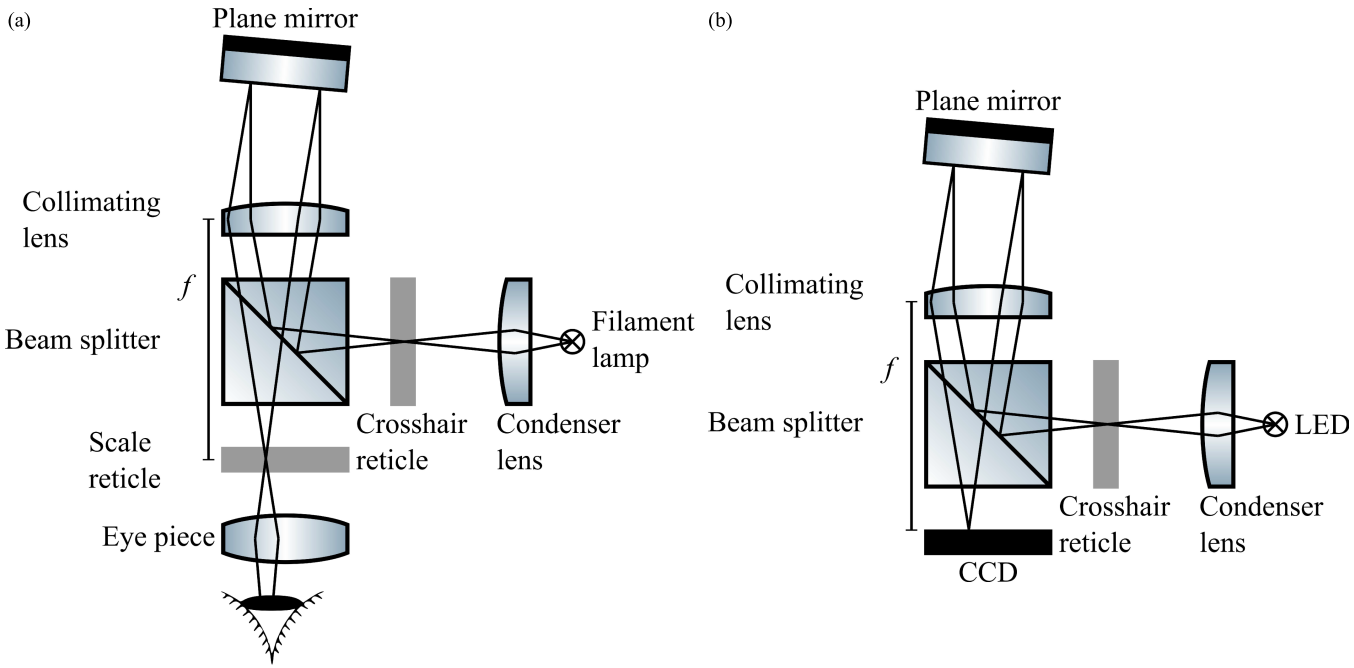

Fig. 1. Schematic of (a) manual autocollimator and (b) digital autocollimator.

parts from digital designs has made 3-D printers an ideal platform for prototyping and building of scientific instruments. By providing the designs of these instruments openly, an ecosystem of similar instruments can flourish with minimal duplication of effort. For example, the OpenFlexure project has produced open source designs for laboratory-grade 3-D printed microscopes [24] and translation stages [25] that can perform precise sub-100-nm scale motion. These stages have been adapted into instruments for both superresolution imaging [26] and modular optomechanics [27]. Cost-effective, customizable, open-source scientific instrumentation is gaining traction in applications ranging from monitoring biodiversity [28] to microfluidics [29]. As an open source 3-D printed instrument, the ACute3D is customizable, low cost, and compact, and it can be integrated directly into other devices. This allows for continuous rather than periodic alignment of angles. By using multiple ACute3Ds with adjusted focal lengths, coarse and fine angular readout could be added to a torsion balance for initial alignment and for coarse feedback control. Furthermore, two ACute3Ds used in conjunction allow for 3-D angle measurement.

II. Design and Alignment

A. Hardware Design

The autocollimator consists of three custom components, all of which are fabricated out of black polylactic acid (PLA) filament using fused filament fabrication 3-D printers. This material has a low thermal expansion coefficient compared to other filaments such as acrylonitrile butadiene styrene (ABS), and the color was chosen to minimize stray reflections. The autocollimator body features a monolithic design that cannot be made through traditional manufacturing methods due to its complex internal geometries. Through compact integration, we were able to reduce the size of the autocollimator, making it stiffer and less susceptible to thermal deformation. Fabricating the main body as a single piece also minimizes the number of parts that needs to be aligned when building the instrument, saving time and effort. Additional items required for the final assembly are standard components widely available on the market, and ThorLabs part numbers are given and were used for our example.

Our autocollimator assembly uses a collimated laser diode (CPS532-C2) as the light source and a Sony IMX219 camera sensor included in a Raspberry Pi camera as the photodetector (see Fig. 2). The laser beam reflected by a plane mirror is attenuated by an absorptive Neutral Density (ND) filter (NE40B) and focused on the camera using a 50-mm focal length achromatic doublet (AC127-050-A). This collimating lens has a diameter of 12.7 mm and is antireflection coated to reduce reflectance over the 400–700 nm range to below 0.5%. A microscope slide is used as a beam splitter to separate the optical path of the outgoing and reflected beams. To avoid interference from stray reflections, a beam dump is used to trap the outgoing beam reflected away from the camera, and the ND filter is tilted by 5° relative the achromatic lens.

We used a standard microscope slide as a plate beam splitter because of its low cost and convenience to incorporate into a compact design. Like all plate beam splitters, the microscope slide exhibits ghosting and interference effects due to secondary reflection on the rear surface. Interference between the similarly angled primary and secondary reflections produces a fringe pattern, where the fringe spacing depends on the parallelism of the slide surfaces. Microscope slides with the minimum interference were selected from those available by shining a laser beam on the microscope slide at 45° angle of incidence and observing the interference pattern in the light

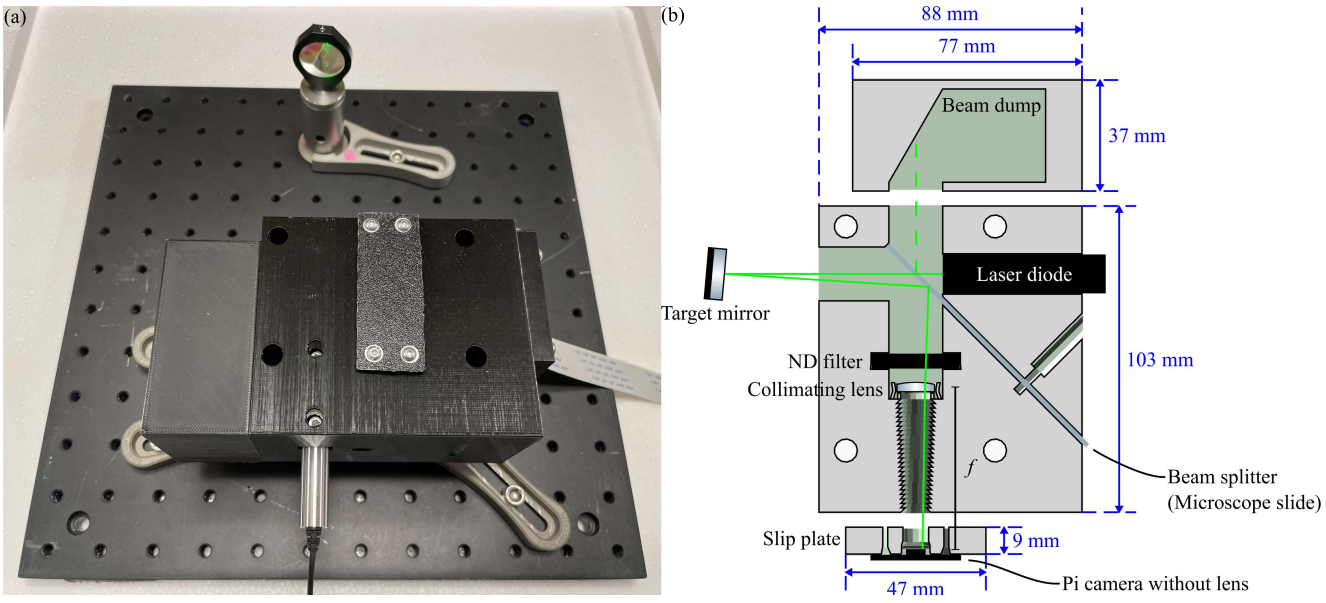

Fig. 2. (a) Photograph of an assembled ACute3D mounted onto a breadboard. The breadboard has 25-mm hole spacing. (b) Schematic of the ACute3D design, the distances between parts are exaggerated to allow them to be distinguished.

reflected onto a screen. We were able to select slides where the fringe pattern was not be visible to the naked eye.

The dimensional accuracy of the printed components depends on the calibration accuracy of the 3-D printer. Angular tilt in the printing axis can introduce errors in the orientation of the laser diode and the microscope slide beam splitter, resulting in a zero position offset. To correct this, we designed a slip plate for the camera module that allows 1 mm of position adjustment about its primary position. Furthermore, inconsistences in the thickness of each printed layer can cause an error in the separation between the collimating lens and the camera sensor. This error was corrected through shimming, see Section II-C for more detail. Manufacturing errors in the outer dimensions of the main body and manufacturing errors in the other printed components do not influence the performance of the autocollimator.

B. Software Design

The software is written in Python using standard scientific Python packages [30]–[34] and runs on a Raspberry Pi. We include an interactive calibration procedure with step-by-step instructions to help the user setup the autocollimator on first use. At the end of this process, the data collected is automatically processed to generate a calibration report and a calibration settings file. Once the autocollimator is calibrated, it can take angular measurements either automatically or manually. The automatic measurement mode continuously outputs the measured angle based on the peak spot position in each captured frame. It is ideal for collecting data at a constant frequency in long experiments that do not require intervention once started. The manual measurement mode measures the angle for 10 s when instructed and outputs an average. It is ideal for experiments that require the measurement noise in the data to be averaged out. In both measurement modes, the peak position of the light spot in every frame captured by the camera is saved to a file in the background. It is easy to integrate the manual measurement mode into an experiment routine, for example, the interactive straightness measurement procedure described in Section V.

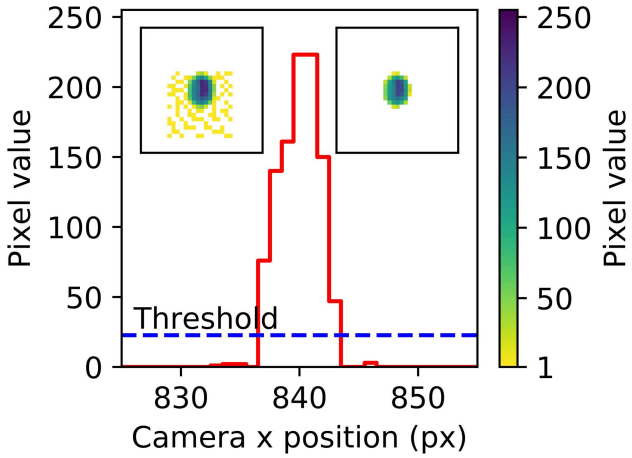

Fig. 3. Intensity distribution horizontally across the center of a laser spot captured in an example 1640 × 1232 pixel frame and the threshold applied to remove background. The top left inset shows all high pixels in the original frame, and the top right inset shows the same frame after the pixels below the threshold have been set to zero. Both insets are 30 × 30 pixels in size, and white represents zero pixel value.

The laser spot is tracked by performing a center of mass operation on the green channel of each captured frame. Each captured frame is an 8-b RGB image with a maximum pixel intensity of 255. To avoid pixel saturation, a neutral density filter is used to attenuate the green laser beam and the background light by a factor of 10^4. Fig. 3 shows the laser spot captured in an example frame. Our software automatically adjusts the shutter speed during initialization to keep all pixel values below 230. The background noise in the frames is

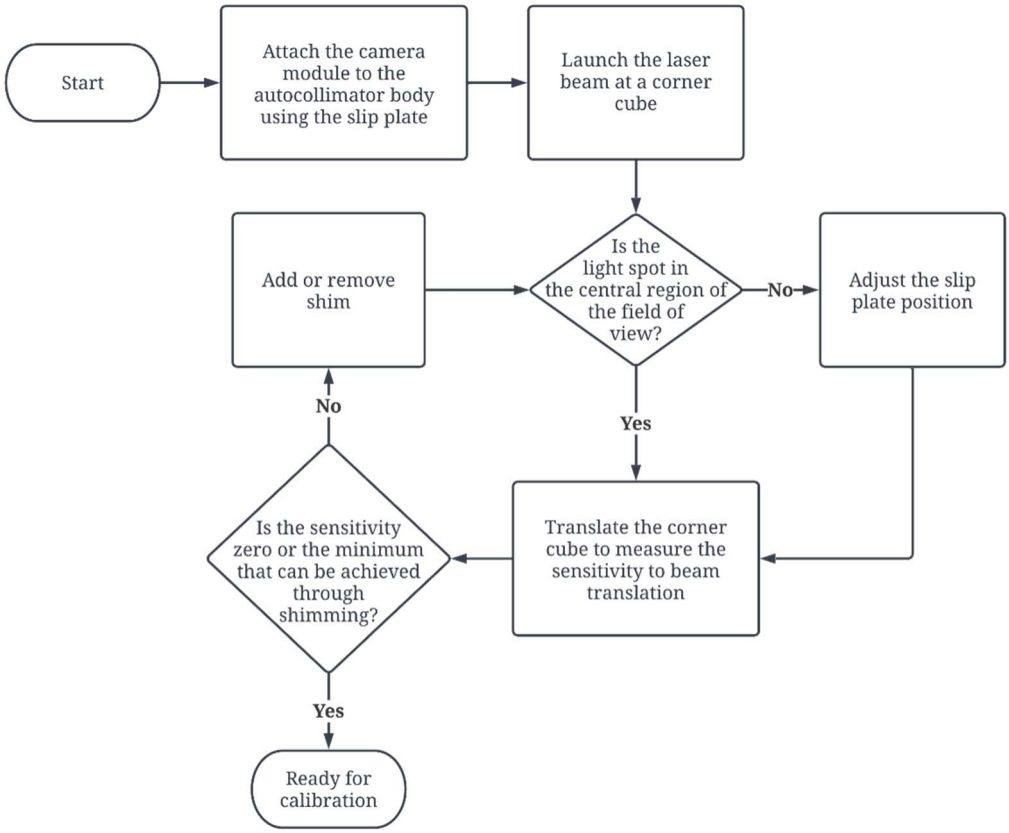

Fig. 4. Flowchart showing the camera alignment procedure using a corner cube mounted on a translation stage.

removed by performing image thresholding. In this process, the intensity of each pixel in the captured image is compared with a threshold value. If the pixel intensity is above the threshold, it is set to the difference between the pixel and threshold values; otherwise, it is set to 0. Shutter speed adjustment and thresholding reduce the spot radius on the camera to around 10 pixels. The threshold value is adaptively selected on a test image captured at startup. This threshold selection algorithm is detailed in our data archive [35]. It was originally developed for a distance sensor [36], and the full algorithm will be discussed in more detail in a separate publication.

C. Camera Alignment

An ideal autocollimator requires a perfectly collimated laser source, and the separation between the collimating lens and the detector needs to be exactly one focal length. If these two conditions are not satisfied, the angle measured by the autocollimator is not only a function of the angle of the target reflector but also a function of beam displacement. We aligned the position of the camera sensor by following the procedure shown in Fig. 4. The starting separation between the back of the achromatic doublet and the camera sensor was found by shimming a mounting tube while imaging an object several meters away outside a window. A sharp image was captured at 46.9 mm, and this value was used to design the autocollimator. We optimized this separation using 0.2-mm shims, the same as the layer thickness used to fabricate the autocollimator. At each increment, the peak spot position was measured before and after an 8-mm beam displacement about the center of the collimating lens. The experimental setup used a corner cube (PS975-A) attached to a XYZ translation stage (PT3/M) as the target reflector. According to ThorLabs specifications, the reflected beam generated by this corner cube is parallel to the incident beam to within 3 arcsec. Without any shims, the sensitivity to translation was 4.5 pixel/mm, decreasing to -0.43 pixel/mm for 0.4 mm. The change in sign indicates that further shims will lead to a greater sensitivity to displacement, so we fixed the camera position using 0.4 mm of shim. The total lens-to-camera separation after shimming is 47.3 mm. This is 0.1 mm longer than the nominal back focal length of the achromatic doublet specified by ThorLabs. The difference is due to the 0.2-mm layer height of the 3-D printer and error in the measured height of the camera sensor above the printed circuit board, which is the mechanical interface with the autocollimator body.

The angle of the camera about the optical axis was aligned by eye. Tilt about the other two Cartesian axes was fixed by mounting the camera module to the slip plate. As the camera sensor is only 3.76 mm across, it needs to be tilted by more than 3° to be out of plane by more than 0.2 mm.

III. Calibration

A. Zero Position

The zero position of our example autocollimator was 848.5 ± 1.1 pixel in x and 540.8 ± 1.5 pixel in y, measured using a corner cube (PS975-A). The uncertainty in the zero

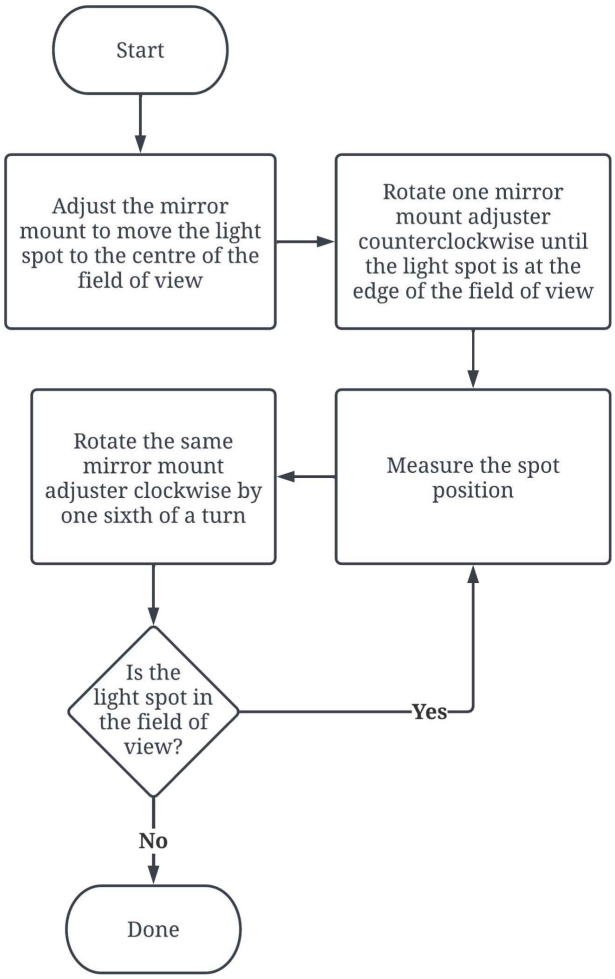

Fig. 5. Flowchart showing the calibration procedure using a mirror mount. Each calibration step is generated by manually turning a hex key into a mechanical stop. This procedure is repeated multiple times for yaw and pitch.

position is characterized by the standard deviation of three sets of repeated measurements, and each set of measurement consists of two readings taken with the reflected beam at opposite edges of the collimating lens.

B. Sensitivity

The position of the light spot on the camera was calibrated against a POLARIS-K1 mirror mount by following the procedure shown in Fig. 5. The angle of the mirror mount was adjusted by manually turning a hex key clockwise into a mechanical stop in steps of 240 $\pm$ 20 arcsec. This step size corresponds to one sixth of a revolution of the adjustment screw on the mirror mount. At each step, the position of the light spot was monitored for 10 s and the average peak spot position was saved as a function of the cumulative change in mirror angle. We did not perform a lens distortion calibration before the system calibration because the camera sensor is very small compared to the focal length of the collimating lens, so the sensor is in a region with minimal field curvature. The camera sensor chip is very flat. Some distortion is possible due to the pitch offset between the pixels and the lenslet array on the IMX219 camera sensor. This will be up to around one pixel at the edges to ensure that light is correctly focused onto each pixel when using the stock lens [37].

C. Analysis

We calibrated our autocollimator in ambient conditions at a working distance of 25 mm. The working distance is the shortest separation between the autocollimator and the target mirror. Due to the 240-arcsec step size and the aperture limitations, the calibration was performed over a range of 6978 arcsec in yaw and 5294 arcsec in pitch. The experiment was made up of three repeated yaw calibrations and three repeated pitch calibrations. For each calibration run, the mirror angles and the peak spot positions were adjusted to be centered at the calibration point closest to the autocollimator zero position measured using the corner cube. From the x and y coordinates of the centered peak positions, we calculate the magnitude of the spot displacement to reduce from 2-D to 1-D. The sign of the displacements is adopted from the x coordinate of the centered peak positions in yaw calibration and the y coordinate of the centered peak positions in pitch calibration. We calibrate the spot displacements against the centered mirror angles by performing a linear fit over calibration points that lie within the central third of the camera sensor. This ensures that the autocollimator is the most accurate when measuring small angles over the region where the system is the most linear. The gradient of the calibration lines is the calibration factor between angular displacement and pixel displacement. The data collected in yaw and pitch calibrations are analyzed separately, as shown in Fig. 6, and the difference between the centered mirror angles and the autocollimator angle calculated using the calibration factor is also shown. It is worth noting that each graph in the figure contains three datasets collected over the repeated calibration runs, and this is not apparent in the top two graphs due to the overlap of data points. The gradient of the calibration line is 0.222084(66) pixel/arcsec in yaw and 0.221786(63) pixel/arcsec in pitch, with uncertainties estimated from the covariance matrix. However, the uncertainty values from the linear fits clearly underestimate the calibration uncertainty because the measurement error of each calibration point and the nonlinearities in the system are not taken into consideration. The difference in the magnitude of the two calibration factors is a more accurate estimate of the calibration error. Since the difference in the magnitude of the calibration factors is 0.1%, we use the average 0.2219(1) pixel/arcsec as the magnitude of the calibration factor. The misalignment between the orientation of the mirror mount and autocollimator axes is less than 1°. This is not a problem because using the total spot displacement ensures that we always work aligned with the mirror axes.

The EURAMET Calibration Guide outlines some accepted procedures on the calibration of autocollimators for authorizing a calibration certificate [38]. Since the aim of our calibration was to get a baseline understanding of performance, we did not follow every guideline. Our method uses a mirror mount, which is a standard piece of equipment in every optics laboratory that can generate small angles traceable to the ratio of two lengths. However, the accuracy of the calibration relies on the resolution of the mirror mount used and the

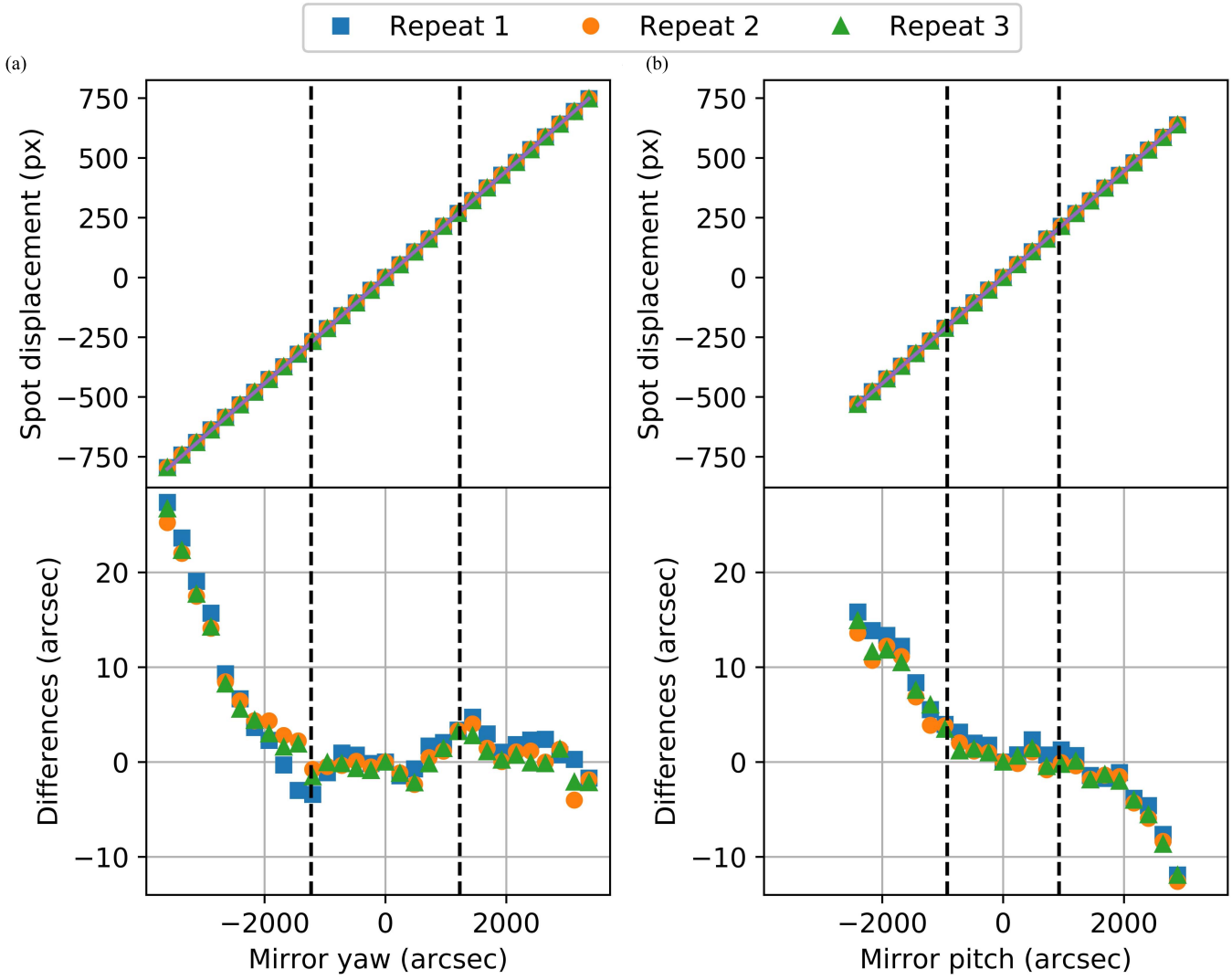

Fig. 6. Calibration between the spot displacements on the camera against (a) yaw and (b) pitch of a Polaris mirror mount. In each of the top graphs, a straight line is fitted to the calibration points within the middle third of the maximum measurement range marked by the dotted lines. The bottom graphs show the difference between the calibration points and the calibration line.

precision of the threads on the adjuster screws. The calibration accuracy is also dependent on the skill of the operator when making each angle adjustment. Manual angle adjustment using a hex key and a mechanical stop transfers the uncertainty in turning an adjuster directly into an uncertainty in the vertical displacement of the hex key lever. Although displacing a long lever is more accurate than turning an adjuster knob directly, the uncertainty in lever displacement ultimately transfers back as a tangent error in the angle of rotation of the adjuster. Over each complete turn of the adjuster knob, the error in individual moves cancels out. We believe that more accurate calibration is possible using automated equipment in a more sophisticated procedure [39]–[44].

IV. Characterization and Performance

A. Measurement Uncertainty

To characterize the measurement uncertainty of the calibrated autocollimator, the calibration experiment is repeated at four different working distances: 23 ± 2 mm, 102 ± 2 mm, 247 ± 2 mm, and 372 ± 2 mm. The experiments were performed in ambient conditions by following the same procedure as the original calibration. Between the original calibration at 25-mm working distance and the calibration at 23-mm working distance, the screws on the mirror mount were loosened to allow the calibration to be repeated using a different section of the threads. All other calibration experiments were carried out using the central section of the adjustment screws on the mirror mount. For each working distance, the pairwise differences between autocollimator angles and the centered mirror angles are averaged between repeated calibration runs and plotted in Fig. 7.

As shown in Fig. 7(a) and (b), the datasets collected at all working distances exhibit a similar trend over the same order of magnitude. This indicates that the threading of the adjuster screw on the mirror mount is not a source of error and we are indeed measuring the nonlinearity of the instrument itself.

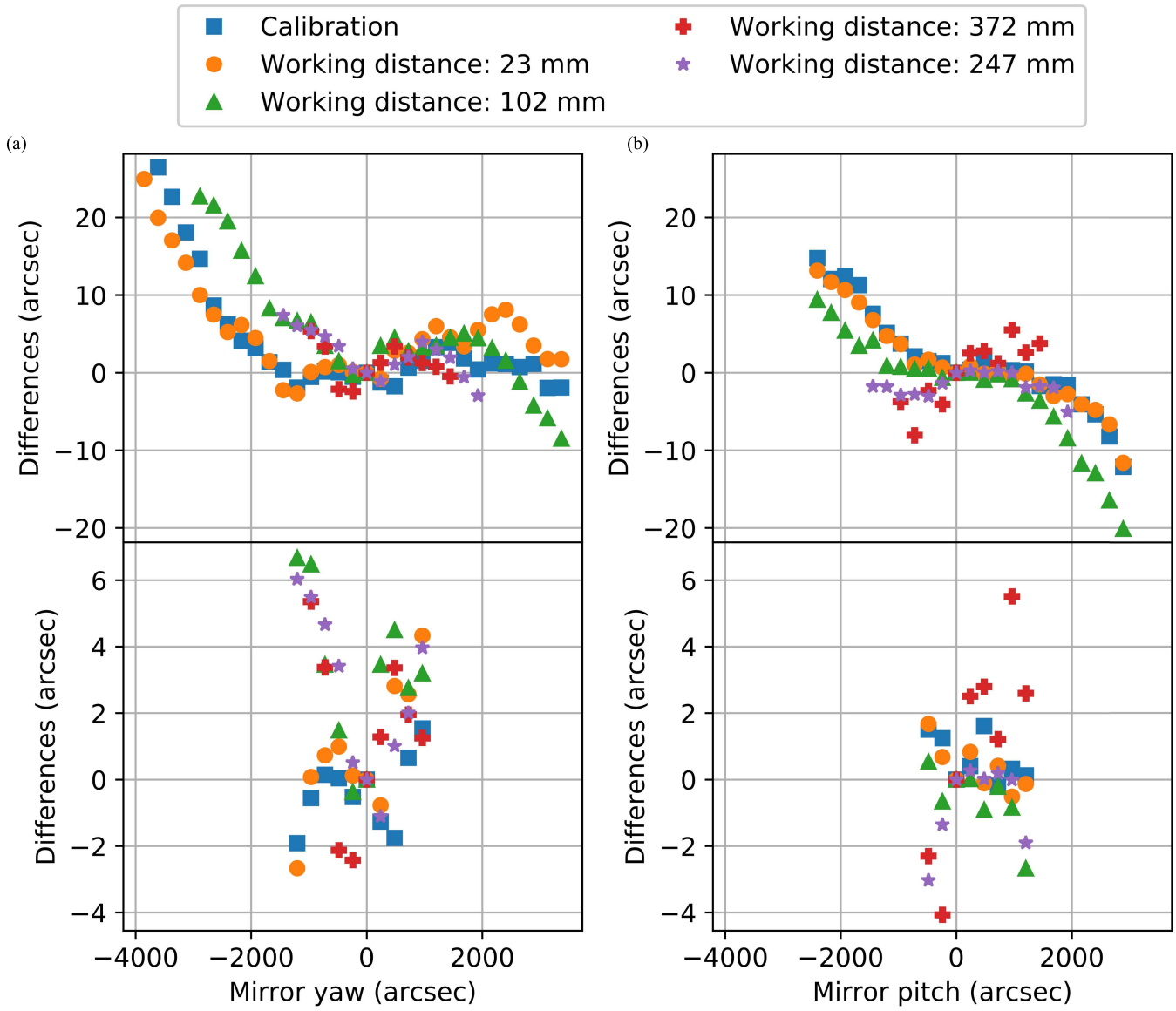

Fig. 7. Difference between the measured autocollimator angle and the expected mirror angle in (a) yaw and (b) pitch over the measurement range of various working distances. Each bottom graph shows a subset of the data points obtained using the middle third of the camera sensor. The data used to plot this graph were collected over a time span of 59 days. Each data point represents the mean of measurements taken over three repeated runs of the experiment.

For each dataset, the differences show the most linear trend over the central third of the maximum measurement range. Near the extremes of the measurement range, nonlinearity builds up in the system due to factors such as beam clipping. Moving part of the beam beyond the aperture of the collimating lens reduces the amount of signal reaching the camera, and the asymmetric spot profile has a detrimental effect on tracking accuracy. Furthermore, the error caused by beam displacement also increases with the magnitude of the angle being measured. This effect is amplified at longer working distance because the beam displacement on the collimating lens for a given angle increases with working distance.

The standard deviation of each dataset plotted in Fig. 7 is used to estimate the measurement uncertainty to $K = 1$ confidence level, as shown in Table I. The pitch difference standard deviation over the middle third of the maximum measurement range shows an increase with the measurement distance. This trend can also be seen in the bottom graph of Fig. 7(b), and the dataset at 372-mm working distance clearly shows the steepest gradient compared to other datasets. This is an indication that the initial calibration factor is inadequate at such a long working distance and the autocollimator should be recalibrated.

The performance of our autocollimator is comparable to the ELCOMAT vario D 90/40 electric autocollimator, which is capable of ±3-arcsec accuracy over an 8170 arcsec by 6840-arcsec measurement range at 200-mm working distance. The difference in performance is mainly caused by the collimating lens, and the ELCOMAT autocollimator uses a 90-mm focal length lens with a clear aperture of 16 mm. The main advantage of our design is customizability, and the lens parameters can be easily modified in the parametric CAD

TABLE I
MEASUREMENT UNCERTAINTY IN YAW AND PITCH AT DIFFERENT WORKING DISTANCES OVER THE FULL AND THE MIDDLE THIRD OF THE MEASUREMENT RANGE

Working distance (mm)	Yaw difference standard deviation (arcsec)		Pitch difference standard deviation (arcsec)	
	Centre ± 1200 arcsec	*Full range [Range (arcsec)]*	*Centre ± 860 arcsec*	*Full range [Range (arcsec)]*
23	2.4	6.4 [± 3600]	1.2	6.6 [± 2600]
102	2.8	7.7 [± 3100]	1.8	7.6 [± 2600]
247	2.4	2.9 [± 1700]	2.7	3.0 [± 1700]
372	2.6	2.6 [± 1200]	3.9	4.7 [± 1200]

file for the autocollimator to house a different collimating lens.

Although the data shown in Fig. 7 are collected over a time span of 59 days, the effect of zero position drift on measurement uncertainty is not shown. This is because the data collected at each working distance are individually centered at the calibration point closest to the autocollimator zero position measured using a corner cube. The drift of the autocollimator is discussed in Section IV-B.

B. Drift

The drift of our autocollimator was characterized under three different thermal conditions. During each experiment, a time series of yaw, pitch, and laboratory temperature were recorded, and the temperature was monitored using an Adafruit temperature sensor (SHT31-D). Care was taken to always startup the autocollimator and allow it to rest in the laboratory for 24 h for warming-up and temperature adaptation before taking any data. The experimental setup is shown in Fig. 8(d), and a corner cube is used as the target reflector to isolate the drift of the autocollimator from the drift of other components in the setup.

Over 43 h in ambient conditions, the laboratory temperature smoothly varied between 25 °C and 27 °C. During this time, the average yaw drift is 0.33 arcsec over any given hour and 2.4 arcsec over any 24-h period. The average pitch drift is 0.26 arcsec over any given hour and 1.9 arcsec over any 24-h period.

Maintaining the laboratory temperature using a domestic air conditioning unit periodically fluctuated the temperature between 20 °C and 23 °C. Over 43 h, the drift in yaw showed negative correlation with temperature with a phase lag as illustrated by the inset in Fig. 8(b). This inset shows yaw and temperature measured over a 10-h period at the middle of the air-conditioned dataset. The drift in pitch is positively correlated with temperature with a less pronounced oval. For 1 °C of temperature variation, the drift in yaw is 1.90 arcsec and the drift in pitch is 1.64 arcsec. These values correspond to less than 0.03% the maximum measurement range in each direction.

Placing the autocollimator in a polystyrene box reduced the effect of temperature cycling, allowing the temperature to be stabilized to less than half a degree Celsius. Over 51 h, the average yaw drift is 0.17 arcsec over any given hour and 0.64 arcsec over any 24-h period. The average pitch drift is 0.11 arcsec over any given hour and 0.22 arcsec over any 24-h period.

To further characterize the drift over different time scales, we calculate the Allan deviation of yaw, pitch, and temperature. Allan deviation is widely used for measuring oscillator frequency stability, and it is a statistical metric of deviation over a characteristic time period τ [45], [46]. For a dataset $x(t)$, the data are divided into M blocks of length τ, and the mean of these blocks is calculated as follows:

$$\bar{x}_i = \int_{(i-1)\tau}^{i\tau} x(t)dt. \tag{1}$$

The Allan deviation for a given τ is the mean squared difference between adjacent blocks

$$\sigma_A(\tau) = \sqrt{\frac{1}{2(M-1)} \sum_{i=1}^{M-1} (\bar{x}_{i+1} - \bar{x}_i)^2}. \tag{2}$$

Fig. 8(a)–(c) shows the Allen deviation of yaw, pitch, and temperature for each of the three datasets collected under different thermal conditions. The average data acquisition interval was 1.028 ± 0.032 s. The difference in time between adjacent data points was caused by jitters in processing times and periodic frame saving, and every 100th captured frame was saved to assist debugging. As Allan variance calculation requires a constant data acquisition interval, the average data acquisition interval is used.

In ambient conditions, the measurement noise averages out over a time scale of 35 s for yaw and 45 s for pitch. Over longer time scales, the Allan deviation is dominated by drift due to temperature changes. At time scales longer than 1 h, the gradient of Allan deviation in log-log space is 0.54 for yaw and 0.60 for pitch. Both gradients are close to 0.5, indicating random walk.

Under cyclic temperature changes, the Allan deviation of yaw and pitch is each separated into three sections by two minima. Prior to the first minimum, the Allan deviation is dominated by measurement noise. This section shows a decreasing trend as the noise is averaged out over a time scale of 3.1 s. In between the two minima, the Allan deviation is dominated by the effect of periodic variation due to temperature. Since the period is not constant, sharp falls over time scales equal to integer multiples of the period are not seen. The maximum in this section implies that the period of

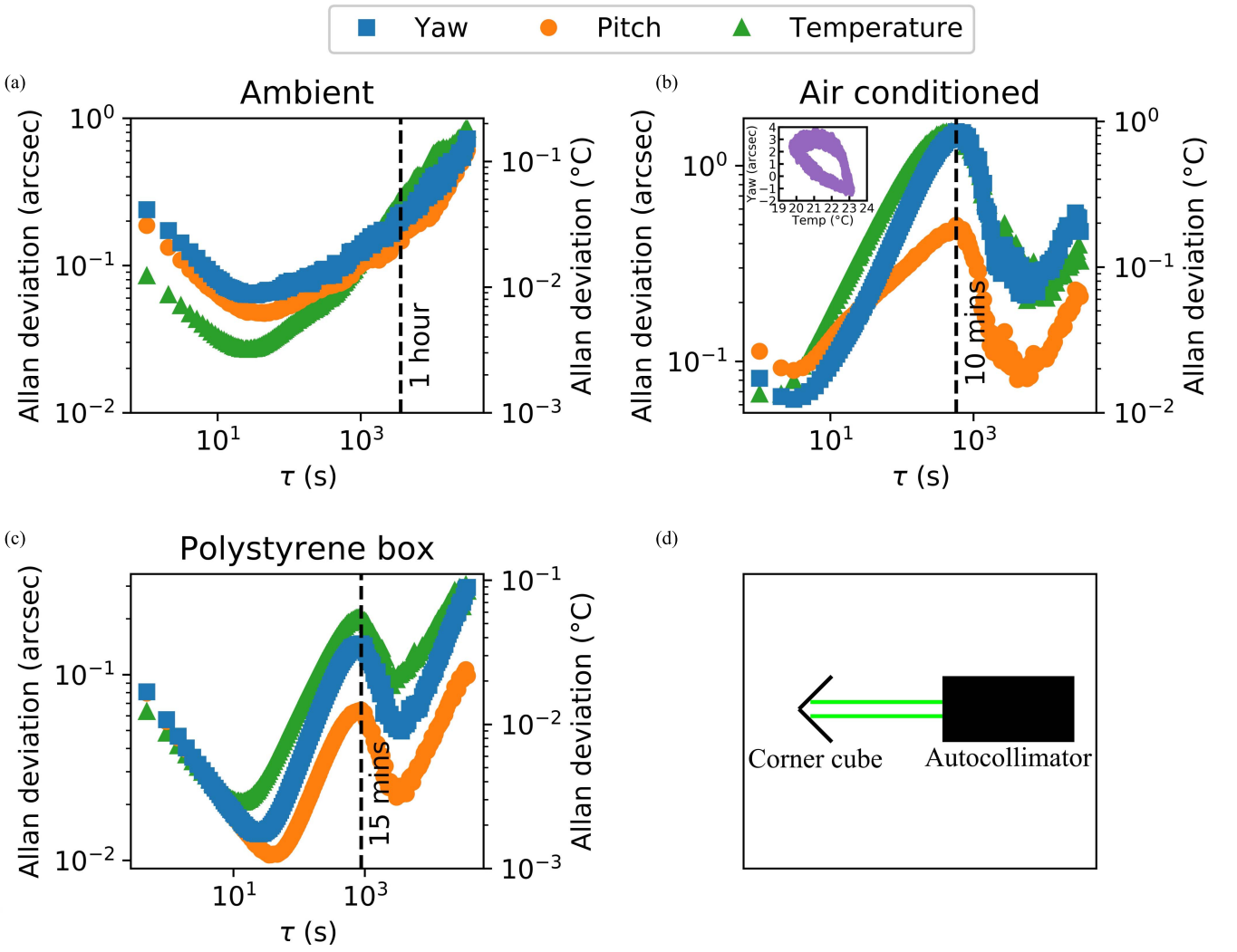

Fig. 8. (a) Allan deviation of the drift data measured over 43 h in ambient conditions. (b) Allan deviation of the drift data measured over 43 h under temperature cycling. The inset shows the correlation between drift in yaw and the laboratory temperature. (c) Allan deviation of the drift data measured over 51 h with the autocollimator placed in a polystyrene box. (d) Experimental setup using a corner cube as the target reflector. The labeled peaks in (b) and (c) indicate that the period of temperature cycling is approximately 20 and 30 min, respectively. The period was set by the air conditioning unit depending on the external temperature.

temperature fluctuation is around 20 min. Beyond the second minimum, the Allan deviation increases due to drift. Placing the autocollimator in a polystyrene box reduced the effect of temperature cycling. However, the drift in yaw is still slightly worse over a time scale of 15 min compared to the dataset collected in ambient conditions because of the periodic temperature variation. A highly specified metrology laboratory would be able to do better temperature stabilization to improve the performance further.

V. Application

We used our autocollimator to measure the angular deviation along one axis of a modular ThorLabs XYZ translation stage (PT3/M). The linear stage being characterized is at the bottom of the assembly and it is oriented to displace along the direction of the laser beam exiting the autocollimator. The experimental setup is shown by the inset in Fig. 9. A plane mirror attached to the translation stage assembly is used as the target reflector, so the measured deviation of the spot indicates angular deviation of the stage. When the linear stage is at zero position, the plane mirror is the furthest away from the autocollimator at a working distance of 93 mm. This working distance is within the range where autocollimator is the most accurate.

The angular deviation of the linear stage was characterized over the 25-mm travel range in steps of 5 mm. At each step, the yaw and pitch of the plane mirror relative to the autocollimator were measured for 10 s. The average of the measurements taken over this period was recorded as a function of stage position. This experiment was repeated three times, and each repeat started from the zero position of the stage. The pairwise difference between the angles measured at each stage position and the angles measured at the zero stage position is averaged between repeats and plotted in Fig. 9.

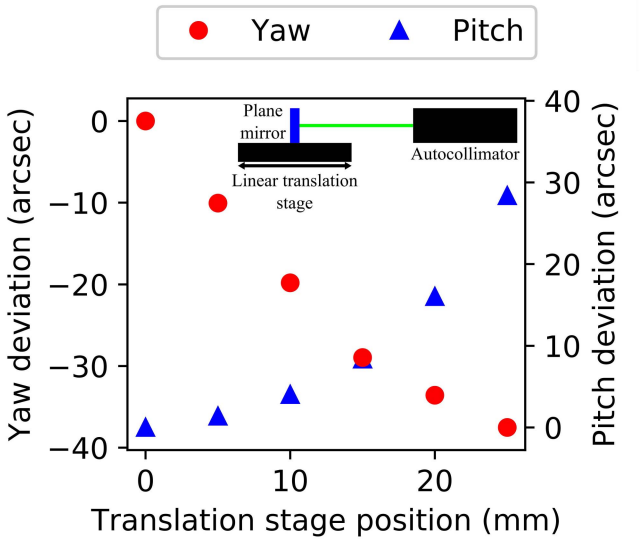

Fig. 9. Angular deviation of a linear translation stage measured at 5-mm intervals over the travel range. The insert shows the experimental setup. Each data point shows the average angular deviation over three repeated runs of the experiment. The error on the angular deviations is propagated from the standard deviation of the repeated angle measurements and indicated using error bars.

The standard deviation estimated from the difference between the angles recorded in each run of the experiment and their corresponding average over the three repeats is 0.57 arcsec for yaw and 0.36 arcsec for pitch. To minimize measurement error, the experiment is performed using the middle third of the camera sensor where the autocollimator is the most linear. However, error sources such as human error in manual stage position adjustments and environmental error due to ambient temperature variations are unavoidable.

The total angular deviation of the linear translation stage over its entire travel range is 48.1 $\pm$ 0.7 arcsec, and the standard deviation is propagated from the standard deviations of yaw and pitch. This result agrees with the less than 52-arcsec angular deviation specified by ThorLabs.

VI. Conclusion

This article presents and characterizes the performance of a 3-D printed laser autocollimator that is capable of measuring angles in two orthogonal directions. The ability to form intricate geometries in a single 3-D printed part has enabled us to create a nearly monolithic design that is compact, lightweight, and easy to build. At short working distance, the autocollimator can make precise angle measurement over a maximum measurement range of 7200 arcsec in yaw and 5200 arcsec in pitch. The system is the most linear over the middle third of the measurement range, over which the maximum measurement uncertainty at working distance below 257 mm is 2.8 arcsec in yaw and 2.7 arcsec in pitch. The mechanical stability of the unit is temperature dependent, under temperature stabilization to less than half a degree Celsius variation, and the autocollimator exhibits subarcsec drift in both yaw and pitch directions. We demonstrated an application of the autocollimator by measuring the angular deviation of a linear translation stage, showing that our design is ready for typical laboratory use.

Acknowledgment

For the purpose of open access, the author has applied a creative commons attribution (CC BY) license to any author accepted manuscript version arising.

References

[1] W. Gao, Y. Saito, H. Muto, Y. Arai, and Y. Shimizu, "A three-axis autocollimator for detection of angular error motions of a precision stage," *CIRP Ann.*, vol. 60, no. 1, pp. 515–518, 2011, doi: 10.1016/j.cirp.2011.03.052.

[2] S. Yang, C. Li, and G. Zhang, "Measurement technology for precision machines," in *Precision Machines*, S. Yang Z. Jiang, Eds. Singapore: Springer, 2019, pp. 1–51, doi: 10.1007/978-981-10-5192-0_15-1.

[3] *Examples for Applications of Collimators, Telescopes, Visual and Electronic Autocollimators*, Moller-Wedel Optical, Wedel, Germany, Mar. 2013, p. 40.

[4] R. D. Geckeler, A. Just, M. Krause, and V. V. Yashchuk, "Autocollimators for deflectometry: Current status and future progress," *Nucl. Instrum. Methods Phys. Res. A, Accel. Spectrom. Detect. Assoc. Equip.*, vol. 616, nos. 2–3, pp. 140–146, May 2010, doi: 10.1016/j.nima.2009.11.021.

[5] S. Qian, R. D. Geckeler, A. Just, M. Idir, and X. Wu, "Approaching sub-50 nanoradian measurements by reducing the saw-tooth deviation of the autocollimator in the nano-optic-measuring machine," *Nucl. Instrum. Methods Phys. Res. A, Accel. Spectrom. Detect. Assoc. Equip.*, vol. 785, pp. 206–212, Jun. 2015, doi: 10.1016/j.nima.2015.02.065.

[6] S. J. Thompson, R. Lang, P. Rees, and G. W. Roberts, "Reconstruction of a conic-section surface from autocollimator-based deflectometric profilometry," *Appl. Opt.*, vol. 55, no. 10, p. 2827, Apr. 2016, doi: 10.1364/AO.55.002827.

[7] C. A. Sanchez and B. M. Wood, "Abbe offset measurement in the NRC Kibble balance," in *Proc. Conf. Precis. Electromagn. Meas. (CPEM)*, Denver, CO, USA, Aug. 2020, pp. 1–2, doi: 10.1109/CPEM49742.2020.9191778.

[8] G. A. Shaw *et al.*, "Milligram mass metrology using an electrostatic force balance," *Metrologia*, vol. 53, no. 5, pp. A86–A94, Oct. 2016, doi: 10.1088/0026-1394/53/5/A86.

[9] N. Yan, M. Kühnel, S. Vasilyan, and T. Fröhlich, "Torsion balance-based system for high-precision force measurement in horizontal plane: Part I. Development concept," *Meas. Sci. Technol.*, vol. 29, no. 8, Aug. 2018, Art. no. 084001, doi: 10.1088/1361-6501/aaba1f.

[10] J. Yuan and X. Long, "CCD-area-based autocollimator for precision small-angle measurement," *Rev. Sci. Instrum.*, vol. 74, no. 3, pp. 1362–1365, Mar. 2003, doi: 10.1063/1.1539896.

[11] J. Yuan, X. Long, and K. Yang, "Temperature-controlled autocollimator with ultrahigh angular measuring precision," *Rev. Sci. Instrum.*, vol. 76, no. 12, Dec. 2005, Art. no. 125106, doi: 10.1063/1.2149010.

[12] A. N. Korolev, A. I. Gartsuev, G. S. Polishchuk, and V. P. Tregub, "A digital autocollimator," *J. Opt. Technol.*, vol. 76, no. 10, p. 624, Oct. 2009, doi: 10.1364/JOT.76.000624.

[13] Y. Yin, S. Cai, and Y. Qiao, "Design, fabrication, and verification of a three-dimensional autocollimator," *Appl. Opt.*, vol. 55, no. 35, p. 9986, Dec. 2016, doi: 10.1364/AO.55.009986.

[14] Y. Guo, H. Cheng, Y. Wen, W. Zhang, and J. Zhu, "High-frequency small angle measurement using a dynamic autocollimator based on an improved K-means algorithm," *Opt. Eng.*, vol. 57, no. 6, p. 1, Jun. 2018, doi: 10.1117/1.OE.57.6.064109.

[15] R. Li *et al.*, "Cube-corner autocollimator with expanded measurement range," *Opt. Exp.*, vol. 27, no. 5, p. 6389, Mar. 2019, doi: 10.1364/OE.27.006389.

[16] E. Hong, "High-accuracy method for measuring two-dimensional angles of a linear guideway," *Opt. Eng.*, vol. 46, no. 5, May 2007, Art. no. 051016, doi: 10.1117/1.2740137.

[17] W. Gao, *Precision Nanometrology*. London, U.K.: Springer, 2010, doi: 10.1007/978-1-84996-254-4.

[18] K. Li, C. Kuang, and X. Liu, "Small angular displacement measurement based on an autocollimator and a common-path compensation principle," *Rev. Sci. Instrum.*, vol. 84, no. 1, Jan. 2013, Art. no. 015108, doi: 10.1063/1.4773004.

[19] S. L. Tan, Y. Shimizu, T. Meguro, S. Ito, and W. Gao, "Design of a laser autocollimator-based optical sensor with a rangefinder for error correction of precision slide guideways," *Int. J. Precis. Eng. Manuf.*, vol. 16, no. 3, pp. 423–431, Mar. 2015, doi: 10.1007/s12541-015-0058-5.

[20] Y.-L. Chen, Y. Shimizu, Y. Kudo, S. Ito, and W. Gao, "Mode-locked laser autocollimator with an expanded measurement range," *Opt. Exp.*, vol. 24, no. 14, p. 15554, Jul. 2016, doi: 10.1364/OE.24.015554.

[21] Y. Guo, H. Cheng, Y. Wen, and Y. Feng, "Three-degree-of-freedom autocollimator based on a combined target reflector," *Appl. Opt.*, vol. 59, no. 8, p. 2262, Mar. 2020, doi: 10.1364/AO.384124.

[22] H. Matsukuma, Y. Asumi, M. Nagaoka, Y. Shimizu, and W. Gao, "An autocollimator with a mid-infrared laser for angular measurement of rough surfaces," *Precis. Eng.*, vol. 67, pp. 89–99, Jan. 2021, doi: 10.1016/j.precisioneng.2020.09.022.

[23] R. Jones *et al.*, "RepRap–the replicating rapid prototyper," *Robotica*, vol. 29, no. 1, pp. 177–191, Jan. 2011, doi: 10.1017/S026357471000069X.

[24] J. T. Collins *et al.*, "Robotic microscopy for everyone: The OpenFlexure microscope," *Biomed. Opt. Exp.*, vol. 11, no. 5, p. 2447, May 2020, doi: 10.1364/BOE.385729.

[25] Q. Meng, K. Harrington, J. Stirling, and R. Bowman, "The OpenFlexure block stage: Sub-100 nm fibre alignment with a monolithic plastic flexure stage," *Opt. Exp.*, vol. 28, no. 4, p. 4763, Feb. 2020, doi: 10.1364/OE.384207.

[26] S. D. Grant, G. S. Cairns, J. Wistuba, and B. R. Patton, "Adapting the 3D-printed openflexure microscope enables computational super-resolution imaging," *FResearch*, vol. 8, p. 2003, Nov. 2019, doi: 10.12688/f1000research.21294.1.

[27] M. Delmans and J. Haseloff, "μCube: A framework for 3D printable optomechanics," *J. Open Hardw.*, vol. 2, no. 1, p. 2, May 2018, doi: 10.5334/joh.8.

[28] A. P. Hill, P. Prince, J. L. Snaddon, C. P. Doncaster, and A. Rogers, "AudioMoth: A low-cost acoustic device for monitoring biodiversity and the environment," *HardwareX*, vol. 6, Oct. 2019, Art. no. e00073, doi: 10.1016/j.ohx.2019.e00073.

[29] A. H. C. Ng, K. Choi, R. P. Luoma, J. M. Robinson, and A. R. Wheeler, "Digital microfluidic magnetic separation for particle-based immunoassays," *Anal. Chem.*, vol. 84, no. 20, pp. 8805–8812, 2012, doi: 10.1021/ac3020627.

[30] C. R. Harris *et al.*, "Array programming with numpy," *Nature*, vol. 585, no. 7825, pp. 357–362, 2020, doi: 10.1038/s41586-020-2649-2.

[31] P. Virtanen *et al.*, "SciPy 1.0: Fundamental algorithms for scientific computing in Python," *Nature Methods*, vol. 17, no. 3, pp. 261–272, Feb. 2020, doi: 10.1038/s41592-019-0686-2.

[32] J. D. Hunter, "Matplotlib: A 2D graphics environment," *Comput. Sci. Eng.*, vol. 9, no. 3, pp. 90–95, May 2007, doi: 10.1109/MCSE.2007.55.

[33] G. Bradski, "The OpenCV library," *Dr Dobb's J. Softw. Tools*, vol. 25, no. 11, pp. 120–125, Nov. 2000.

[34] F. Pezoa, J. L. Reutter, F. Suarez, M. Ugarte, and D. Vrgoč, "Foundations of JSON schema," in *Proc. 25th Int. Conf. World Wide Web*, Montreal, QC, Canada, Apr. 2016, pp. 263–273, doi: 10.1145/2872427.2883029.

[35] Q. Meng, J. Stirling, W. Wadsworth, and R. Bowman, "Dataset for ACute3D: A compact, cost-effective, 3D printed laser autocollimator," Univ. Bath, Bath, Dataset 1141, 2022, doi: 10.15125/BATH-01141.

[36] *GitLab Repository of the Parallax Displacement Sensor*. Accessed: Jan. 16, 2022. [Online]. Available: https://gitlab.com/bath_open_instrumentation_group/parallax-displacement-sensor

[37] R. W. Bowman, B. Vodenicharski, J. T. Collins, and J. Stirling, "Flat-field and colour correction for the raspberry pi camera module," *J. Open Hardw.*, vol. 4, p. 1, no. 1, Apr. 2020, doi: 10.5334/joh.20.

[38] *Guidlines on the Calibration of Autocollimators*, EURAMET, Brunswick, Germany, Jul. 2017.

[39] A. Just, M. Krause, R. Probst, and R. Wittekopf, "Calibration of high-resolution electronic autocollimators against an angle comparator," *Metrologia*, vol. 40, no. 5, pp. 288–294, Oct. 2003, doi: 10.1088/0026-1394/40/5/011.

[40] R. D. Geckeler, O. Kranz, A. Just, and M. Krause, "A novel approach for extending autocollimator calibration from plane to spatial angles," *Adv. Opt. Technol.*, vol. 1, no. 6, Jan. 2012, doi: 10.1515/aot-2012-0048.

[41] R.-E. Precup, S. Kovács, S. Preitl, and E. M. Petriu, Eds., *Applied Computational Intelligence in Engineering and Information Technology Revised and Selected Papers from the 6th IEEE International Symposium on Applied Computational Intelligence and Informatics SACI 2011*, vol. 1. Berlin, Germany: Springer, 2012, doi: 10.1007/978-3-642-28305-5.

[42] B. J. Eves, "The NRC autocollimator calibration facility," *Metrologia*, vol. 50, no. 5, pp. 433–440, Oct. 2013, doi: 10.1088/0026-1394/50/5/433.

[43] V. Heikkinen, V. Byman, I. Palosuo, B. Hemming, and A. Lassila, "Interferometric 2D small angle generator for autocollimator calibration," *Metrologia*, vol. 54, no. 3, pp. 253–261, Jun. 2017, doi: 10.1088/1681-7575/aa648d.

[44] M. Schumann, R. D. Geckeler, M. Krause, and A. Just, "The spatial angle autocollimator calibrator: Optimised model, uncertainty budget and experimental validation," *Metrologia*, vol. 56, no. 1, Feb. 2019, Art. no. 015011, doi: 10.1088/1681-7575/aaee2e.

[45] D. W. Allan, "Time and frequency (time-domain) characterization, Estimation, and prediction of precision clocks and oscillators," *IEEE Trans. Ultrason., Ferroelectr., Freq. Control*, vol. 34, no. 6, pp. 647–654, Nov. 1987, doi: 10.1109/T-UFFC.1987.26997.

[46] M. Vagner, P. Benes, and Z. Havranek, "Experience with Allan variance method for MEMS gyroscope performance characterization," in *Proc. IEEE Int. Instrum. Meas. Technol. Conf.*, Graz, Austria, May 2012, pp. 1343–1347, doi: 10.1109/I2MTC.2012.6229362.

Qingxin Meng received the M.S. degree in physics from the University of Bath, Bath, U.K., in 2018, where he is currently pursuing the Ph.D. degree with Bath Open Instrumentation Group. The main topic of his Ph.D. research is 3-D printed scientific hardware.

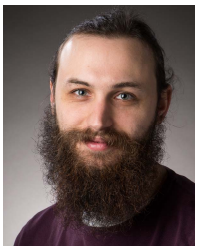

Julian Stirling received the Ph.D. degree from the University of Nottingham, Nottingham, U.K., in 2014, focusing on scanning probe microscopy instrumentation.

He then moved to the U.S. National Institute of Standards and Technology (NIST), Gaithersburg, MD, USA, where he has worked on small force metrology. In 2016, he joined the Joint Quantum Institute, University of Maryland, College Park, MD, USA, where he spent two years in measuring the universal constant of gravitation. Since January 2018, he has been working with the University of Bath, Bath, U.K., where he currently works on the development of open source scientific hardware. His research also focuses on the infrastructure needed for open hardware to enable free knowledge exchange from universities without encumbering innovations with patents.

William J. Wadsworth received the B.A. and D.Phil. degrees from the University of Oxford, Oxford, U.K., in 1993 and 1997, respectively.

He joined the University of Bath, Bath, U.K., in 1999, where he is currently a Professor of photonics. His research interests are the applications of optics, including metrology, laser machining, imaging, and medical and life sciences.

Richard W. Bowman received the Ph.D. degree from the University of Glasgow, Glasgow, U.K., in 2012.

He is currently a Royal Society University Research Fellow and a Proleptic Reader at the University of Bath, Bath, U.K., leading a research group focused on open hardware and optical instrumentation. He leads the OpenFlexure Project, an initiative centered on open source hardware designs for scientific instruments that is now at the center of a global community of users and contributors. His background is in optics and nanoscience, having previously worked as the Queens' College and Royal Commission 1851 Research Fellow at the University of Cambridge, Cambridge, U.K.